



Conjugated poly(benzothiadiazole)/g-C₃N₄ heterojunctions via halogenation for enhanced visible-light photocatalytic selective oxidation of sulfides

Chu Chu, Yuancheng Qin^{*}, Cailing Ni, Nannan Wu, Jianping Zou^{*}

Key Laboratory of Jiangxi Province for Persistent Pollutants Control and Resources Recycle, Nanchang Hangkong University, Nanchang 330063, PR China

ARTICLE INFO

Keywords:

Conjugated polymer
Halogenation
g-C₃N₄
Heterojunctions
Selective oxidation

ABSTRACT

Porous organic polymers have been considered potential materials for synthesizing molecules by selective activation of bonds of visible light photocatalytic catalysis. However, the low charge mobility and weak interface conductivity prohibited further application. Herein, three new polymers with fluorene as donor and benzothiadiazole by halogen substitution (F or Cl) as acceptor unit were successfully synthesized and further constructed heterostructure with g-C₃N₄. DCIB-BTDF/g-C₃N₄ heterojunctions exhibited superior photocatalytic activity for the selective oxidation of sulfides to sulfoxides under visible-light illumination, the highest activity reached > 98 % of conversion in a short time, which was more than two times higher than that of pristine DCIB-BTDF. This is mainly attributed to the enhanced carrier separation efficiency of DCIB-BTDF/g-C₃N₄. Our finding could provide further insights into the design and synthesis of the halogenation strategy of polymer/g-C₃N₄ heterojunctions.

1. Introduction

Visible-light-driven chemical transformations have been recognized as an attractive environment-friendly strategy to synthesize molecules, which have attracted wide attention to explore in the past decades [1–5]. Graphitic carbon nitride (g-C₃N₄) is one of the most popular photocatalysts in recent years because of its excellent photocatalytic properties [6]. A considerable number of researchers have been devoted to promoting the migration and separation of its photoexcited and enhanced the visible light absorption capacity of CN-based catalysts, such as structure defect engineering [7,8], element doping [9,10], dye-sensitization strategy [11,12], building heterojunctions [13,14] and so on. The construction of semiconductor/heterostructure has been widely used in the field of efficient H₂ evolution [15–18], but rarely in photocatalytic organic reactions [19,20].

Porous organic polymers (POPs) are considered as one of the most promising semiconductor materials due to their visible light response and chemical stability [21–25]. POPs are known as their rich porous structure, chemical stability and tunable skeleton. To this regard, outstanding potential has thus been acquired for the development of visible-light-driven chemical transformations such as cross dehydrogenative coupling (CDC) reactions [26,27], oxidative hydroxylation of

arylboronic acids [28,29], photocatalytic hydrogen evolution [30,31] and CO₂ reduction [32,33], but still not enough in the selective oxidation reactions [34].

As we know, aromatic derivatives with benzothiadiazole-based structures have been widely used in organic photovoltaic materials due to their excellent light response capability [35–37]. Thus it might be a feasible approach to improve the photocatalytic performance by introducing the benzothiadiazole structure into POPs. Recently, our group developed a series of XBD-BTTs by using benzothiadiazole, a strong electron absorption unit and introducing heteroatoms (S, F, Cl). Halogenated polymers usually exhibit faster charge-carrier transport due to higher backbone planarity and great oxidation ability due to deeper highest occupied molecular orbital (HOMO) levels [25]. It has been proved that introducing halogen atoms into the polymer can enhance the performance of its photocatalytic C-C coupling reaction.

In addition, constructing polymer heterojunctions (PHJs) were also a promising strategy [38–41]. Ji et al. reported the zinc porphyrin polymer/g-C₃N₄ heterojunction for promoting the oxidative coupling of amines [20]. Gong et al. investigated the effect of the electron-donating ability of D-A polymer/g-C₃N₄ heterojunction on the hydrogen production efficiency [42]. However, the low-efficient charge transfer and weak interface reaction sites limit the photocatalytic efficiency of

^{*} Corresponding authors.

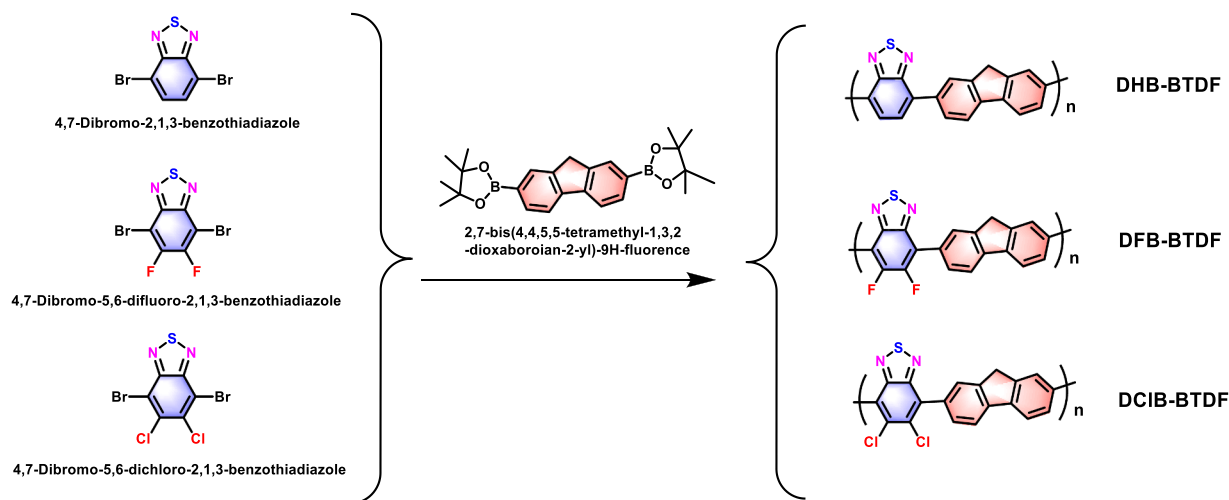
E-mail addresses: qinyuancheng@hotmail.com (Y. Qin), zjp.112@126.com (J. Zou).

<https://doi.org/10.1016/j.apcatb.2023.123321>

Received 7 August 2023; Received in revised form 18 September 2023; Accepted 21 September 2023

Available online 22 September 2023

0926-3373/© 2023 Elsevier B.V. All rights reserved.



Scheme 1. General synthetic routes of DHB-BTDF, DFB-BTDF and DCIB-BTDF.

polymer/g-C₃N₄ in selective oxidation reactions. Therefore, synthesizing a heterojunction between benzothiadiazole-based POPs by halogenated and CN can be a promising strategy for improving the separation of photogenerated carriers and enhancing photocatalytic performance.

To test this hypothesis, we first synthesized a series of donor-acceptor type benzothiadiazole-based conjugated organic polymer DXB-BTDF (X = H, F, Cl) (Scheme 1). The heterojunction photocatalyst of DXB-BTDF/g-C₃N₄ were further assembled via the noncovalent π - π interaction. The addition of g-C₃N₄ can attract and transfer the photogenerated holes of DXB-BTDF, boosting the separation efficiency of electron holes. A series of characterizations thoroughly explored optical and electronic properties. The formation of heterostructure can reduce the band gap to adjust charge separation and transport. DCIB-BTDF/g-C₃N₄ exhibited excellent photocatalytic activity in selective oxidation of sulfides under visible light irradiation, the highest activity of DCIB-BTDF/g-C₃N₄ could be reached to 98 % of conversion, which was more than 2 times higher than that of pristine DCIB-BTDF. Furthermore, photoelectrochemical experiments and the electron paramagnetic resonance (EPR) spectra were employed to propose the possible photocatalytic mechanism, further supporting that the formation of heterostructure and halogenating adjustment accelerated the photocatalytic activity. Our study on DXB-BTDF/g-C₃N₄ heterojunctions photocatalyst provides helpful inspiration to design photocatalysts with high activity for the selective oxidation of sulfides to sulfoxides under visible-light illumination.

2. Experimental section

All the commercially available chemicals were purchased and used directly in analytical purity without further purification, and the 4,7-Dibromo-5,6-difluoro-2,1,3-benzothiadiazole, 4,7-Dibromo-5,6-dichloro-2,1,3-benzothiadiazole and 2,7-dibromo-9 H-fluorene was synthesized according to the reported procedure [43–45].

2.1. Synthesis of DXB-BTDF

General synthesis for Suzuki-Miyaura polymerization procedures (DHB-BTDF): 4,7-dibromo-2,1,3-benzothiadiazole, and 2,7-bis (4,4,5,5-tetramethyl-1,3,2-dioxaborolan-2-yl)-9 H-fluorene (0.4 g, 1 mmol), K₂CO₃ (0.8 g, 6 mmol), 20 mL of toluene were added to a 50 mL round bottom flask, and bubbled for 30 min under argon gas before Pd(PPh₃)₄ (80 mg, 0.04 mmol) and a drop of methyltrimethylammonium chloride was added. Then the mixture was placed under N₂ atmosphere and refluxed to 110 °C for 48 h. After cooling to room temperature, the mixture was filtered through a pad of elite. The

solid was filtered and washed with acetone and THF for three times. The crude product was recovered and dried under vacuum at 60 °C to afford a yellow soild (220 mg), yield 82 %.

2.1.1. DFB-BTDF

brown solid (673 mg), yield 68 %. 4,7-Dibromo-5,6-difluoro-2,1,3-benzothiadiazole (0.45 g, 1 mmol) and 2,7-bis (4,4,5,5-tetramethyl-1,3,2-dioxaborolan-2-yl)-9 H-fluorene (0.4 g, 1 mmol).

2.1.2. DCIB-BTDF

yellow soild (349 mg), yield 46 %. 4,7-dibromo-2,1,3-benzothiadiazole (0.36 g, 1 mmol) and 2,7-bis (4,4,5,5-tetramethyl-1,3,2-dioxaborolan-2-yl)-9 H-fluorene (0.4 g, 1 mmol).

2.2. Synthesis of g-C₃N₄

Pristine graphitic carbon nitride was prepared by thermal polycondensation using urea as the precursor. Typically, 18.0 g urea was placed in a crucible and heated up to 550 °C at a heating rate of 5 °C/min and calcined at 550 °C for 5 h under N₂ atmosphere in a tube furnace. After cooling to room temperature, the yellow g-C₃N₄ was obtained into power.

2.3. Synthesis of polymer/g-C₃N₄ heterojunctions photocatalysts

All polymer/g-C₃N₄ heterojunctions were prepared in the same way. 20 mg DXB-BTDF samples and 80 mg g-C₃N₄ were uniformly dispersed in 80 mL chloroform. The solvent was evaporated in vacuum and dried at 50 °C for 24 h.

2.4. Photochemical and electrochemical measurements

Fourier-transformed infrared (FT-IR) spectra were measured in the range of 4000–400 cm⁻¹ by using KBr disks on an infrared spectrometer by an infrared spectrometer (Vertex, Swiss Bruker Company). Surface areas and pore size distributions (77 K) were measured by nitrogen adsorption and desorption using a Micromeritics ASAP 2020 M surface area and porosity analyzer, and the samples were activated at 110 °C for 10 h under vacuum (10–5 bar) before analysis. Based on N₂ adsorption data, the pore size distribution was calculated from the adsorption branch by the nonlocal density functional theory (NLDFT). For TGA measurements, the temperature was raised from 0 to 800 °C at a rate of 10 °C min under nitrogen atmosphere by Thermogravimetric analysis (TGA) (SDT Q600, American TA Corporation). The microstructures of the catalysts were investigated by field emission scanning electron

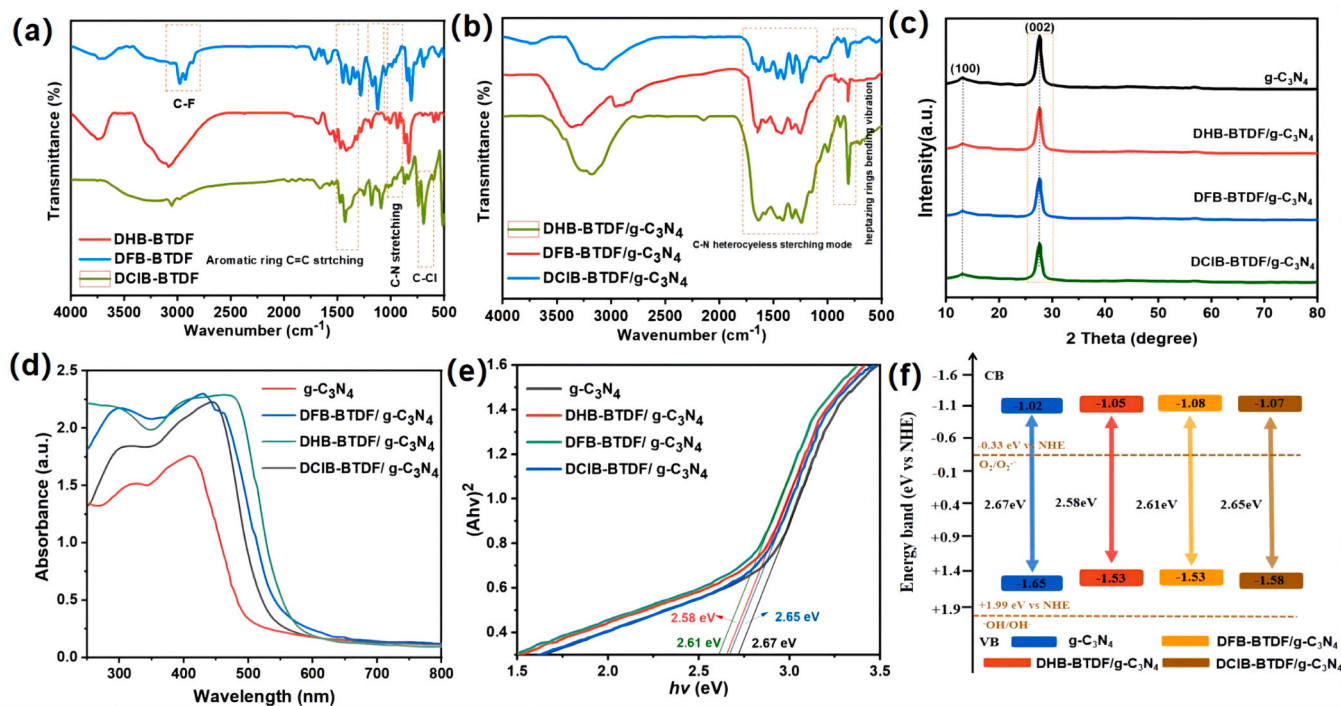


Fig. 1. (a) FTIR spectra of the DXB-BTDF polymers; (b) FTIR spectra of the DXB-BTDF/g-C₃N₄ heterojunction; (c) Powder XRD patterns of the g-C₃N₄, DXB-BTDF/g-C₃N₄ heterojunction; (d) UV-vis diffuse reflectance spectra of the g-C₃N₄, DXB-BTDF/g-C₃N₄ heterojunction; (e) the Tauc plots of Flu-BZ, Flu-FBZ, and Flu-DFBZ; (f) The band positions [redox potentials vs. normal hydrogen electrode (NHE)] of g-C₃N₄ and DXB-BTDF/g-C₃N₄.

microscope (FE-SEM, Quattro ESEM, Thermo Fisher) and high-resolution transmission electron microscope (HR-TEM, JEM-2100 F, JEOL). The electron paramagnetic resonance (EPR) spectra were conducted using a Magnetech Miniscope MS200 spectrometer. X-ray diffraction (XRD) patterns were recorded on a MiniFlex II diffractometer) and operating in a 2θ range of $3-40^\circ$ at a scanning rate of $10^\circ \text{ min}^{-1}$ with Cu-K α radiation ($\lambda = 1.5418 \text{ \AA}$). UV-vis diffuse reflectance (UV-vis-DRS) spectra of the samples were measured under room temperature, over the wavelength range of 200–800 nm by Shimadzu UV-3600 spectrometer (UV-3600, Shimadzu Japan). The transient electrochemical impedance spectra (EIS), Mott-Schottky measurements and photocurrent responses of samples were obtained on a CHI650E electrochemical workstation with a classic three-electrode system (Ag/AgCl as reference electrode, Pt wire as a counter electrode). The photoluminescence (PL) spectra were detected on an FLSP920 fluorescence spectrometer (Edinburgh Instruments, England).

2.5. Electrochemical analysis

All the photoelectrochemical measurements were performed on an electrochemical workstation (CHI650E, CH Instruments Inc., Shanghai). 3 mg of catalyst was dispersed in 2.0 mL absolute ethanol and 100 μL Nafion mixture solution, which was ultrasonically dispersed for 30 min, and then 100 μL of the resultant slurry was dropped onto the ITO glass with $1 \times 3 \text{ cm}^2$ illuminated area and dried at 100°C for 1 h. In all the electrochemical experiments, we assembled the Pt line (counter electrode), Ag/AgCl electrode (reference electrode), and coated ITO conductive glass (working electrode) into a three-electrode system with 0.2 M Na₂SO₄ aqueous solution was used as the electrolyte. The photocatalytic activity reaction was conducted under a blue light LED rack (460 nm) irradiation. The transient photocurrent-time (I-t) was measured using a blue light LED light (460 nm). For EIS, the frequency range was 100–105 Hz and the amplitude was 5 mV at the open circuit voltage. The Mott-Schottky (M-S) plots were measured at frequencies of 500, 1000 Hz and 1500 Hz in the dark. The lowest unoccupied

molecular orbital (LUMO) levels were calculated from the results of Mott-Schottky measurements.

2.6. Photocatalytic activity test

A 10 mL vial equipped with a magnetic stir bar was charged the corresponding sulfide (2 mmol) and 10 mg of catalyst, then added 5 mL of CH₃CN/H₂O (v/v 1:1). The mixture was treated with 30 min of ultrasonication in dark to achieve absorption-desorption equilibrium, and stirred at 1000 rpm and irradiated with a 460 nm blue light LED photoreactor. The reaction mixture was stirred at 25°C . The reaction was monitored by TLC and ¹H NMR. After the total consumption of the sulfide, the crude was filtered through celite and purified by column chromatography. Finally, catalysts were removed by centrifugation. Conversion for the oxidation of sulfides to sulfoxides were defined as follows: Conversion = [Consumed Sulfide]/[Initial Sulfide] $\times 100\%$.

3. Results and discussions

3.1. Photocatalyst characterization

The successful synthesis of g-C₃N₄ and each respective DXB-BTDF were determined and FT-IR further characterized corresponding polymer/g-C₃N₄ heterojunctions analysis. The peaks near 1450 cm^{-1} and 1200 cm^{-1} belong to aromatic ring C=C and C-N stretching vibration respectively. The peak at 3000 cm^{-1} belongs to the C-H stretching vibration, which reveals that the aromatic conjugated D-A skeleton of the polymer has been formed during the polymerization process. As shown in Fig. 1a, Compared to DHB-BTDF, new signals at 750 cm^{-1} in DCIB-BTDF can be assigned to C-Cl bonds and 1230 cm^{-1} in DFB-BTDF can be assigned to C-F bonds (Fig. 1b). The N-H and O-H stretching vibration at 3200 cm^{-1} , the C-N heterocyclic stretching mode at 1240 cm^{-1} to 1650 cm^{-1} and the bending vibration at 811 cm^{-1} at pure g-C₃N₄ and polymer/g-C₃N₄ heterojunctions show that the existence of g-C₃N₄ and the typical structure of g-C₃N₄ are not damaged. In addition, the C-H

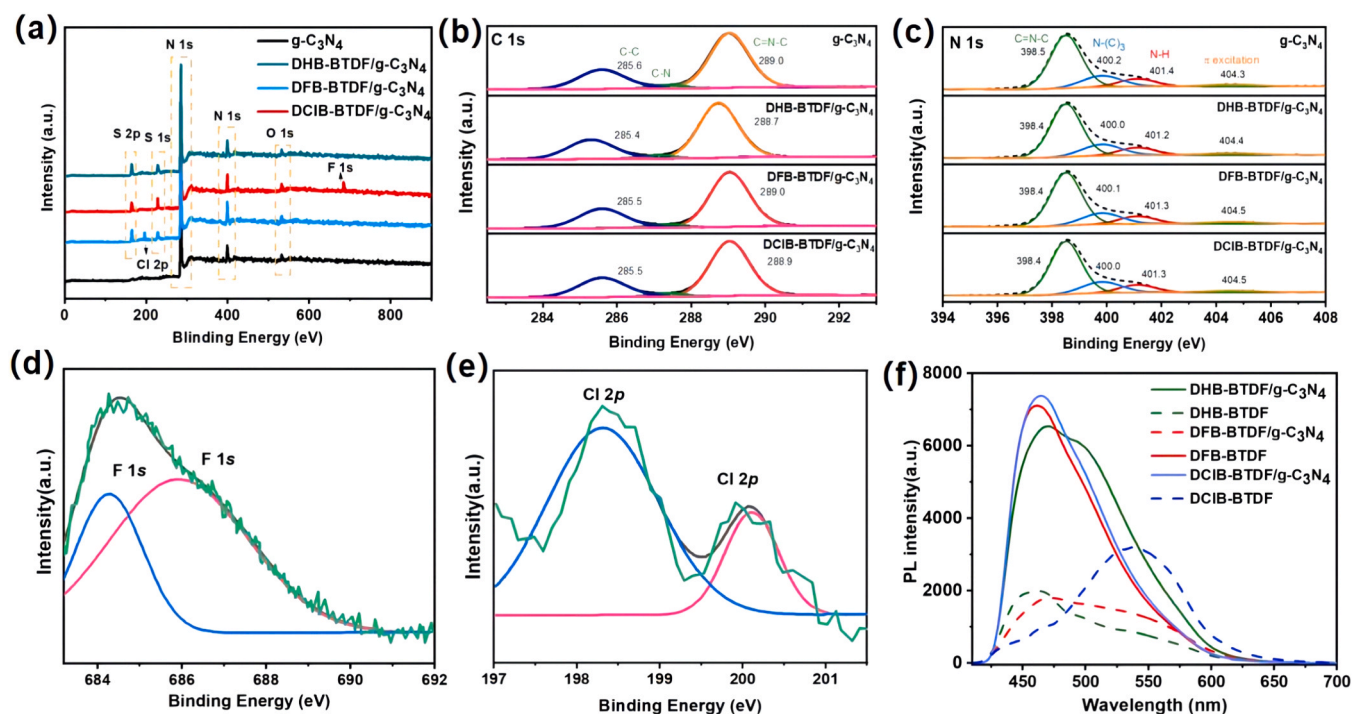


Fig. 2. High-resolution XPS spectra of g-C₃N₄, DXB-BTDF/g-C₃N₄ (X = H, F, Cl) heterojunction: (a) survey; (b) C1s; (c) N1s; (d) F1s of the DFB-BTDF/g-C₃N₄; (e) Cl2p of the DCIB-BTDF/g-C₃N₄. (f) The PL of the DXB-BTDF polymers and DXB-BTDF/g-C₃N₄ heterojunction.

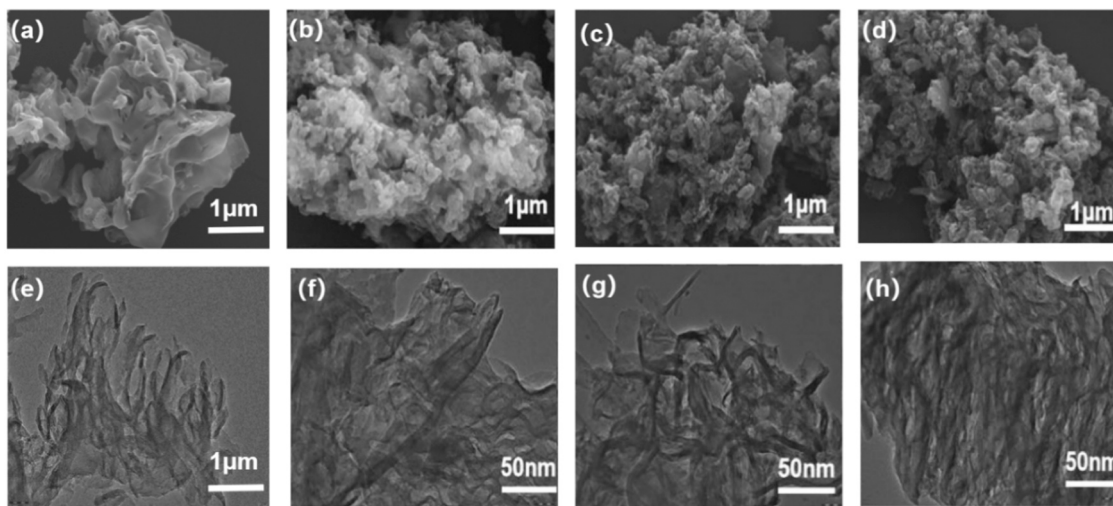


Fig. 3. SEM image of g-C₃N₄ (a), DHB-BTDF/g-C₃N₄ (b), DFB-BTDF/g-C₃N₄ (c), DCIB-BTDF/g-C₃N₄ (d); TEM image of g-C₃N₄ (e), DHB-BTDF/g-C₃N₄ (f), DFB-BTDF/g-C₃N₄ (g), DCIB-BTDF/g-C₃N₄ (h).

stretching vibration at 3000 cm⁻¹ in the polymer/g-C₃N₄ heterojunctions were distributed to the aromatic conjugated chain of the polymer, which confirmed the successful synthesis of the heterojunctions.

The PXRD pattern of the DXB-BTDF shows a typical broad peak [46] demonstrating the formation of non-ordered amorphous polymer through solvothermal condition in Fig. S1(a). With the introduction of g-C₃N₄, all samples had two identical diffraction peaks at 13.0° and 27.7°, which were attributed to the in-plane repeat period in (100) and interlayer stacking of aromatic systems in (002) for g-C₃N₄ (Fig. 1c). This result indicated that the compound process of D-A conjugated polymer did not change the main structure of g-C₃N₄.

Light absorption played a crucial role in the photocatalytic activity of

photocatalysts. Hence, the optical properties of g-C₃N₄ and polymer/g-C₃N₄ heterojunctions were characterized by UV–visible diffuse reflectance spectroscopy (DRS). As shown in Fig. S1(b), all polymers behave in a broad visible-light response spectrum from 300 to 600 nm. In addition, three polymer/g-C₃N₄ heterojunctions showed a wider visible light response spectrum from 200 nm to 600 nm compared to unloaded g-C₃N₄ (Fig. 1d), and the blue-shift is obvious with the incorporation of F atoms and Cl atoms into the benzothiadiazole receptor unit of the polymer skeleton. DCIB-BTDF/g-C₃N₄ even shifts to 600 nm. This blue shift may be attributed to intramolecular charge transfer (ICT) caused by the inherent donor-receptor characteristics in the halogenated polymer framework [47–49]. The three heterojunction polymers show excellent visible light capture ability, indicating that the heterojunction structure

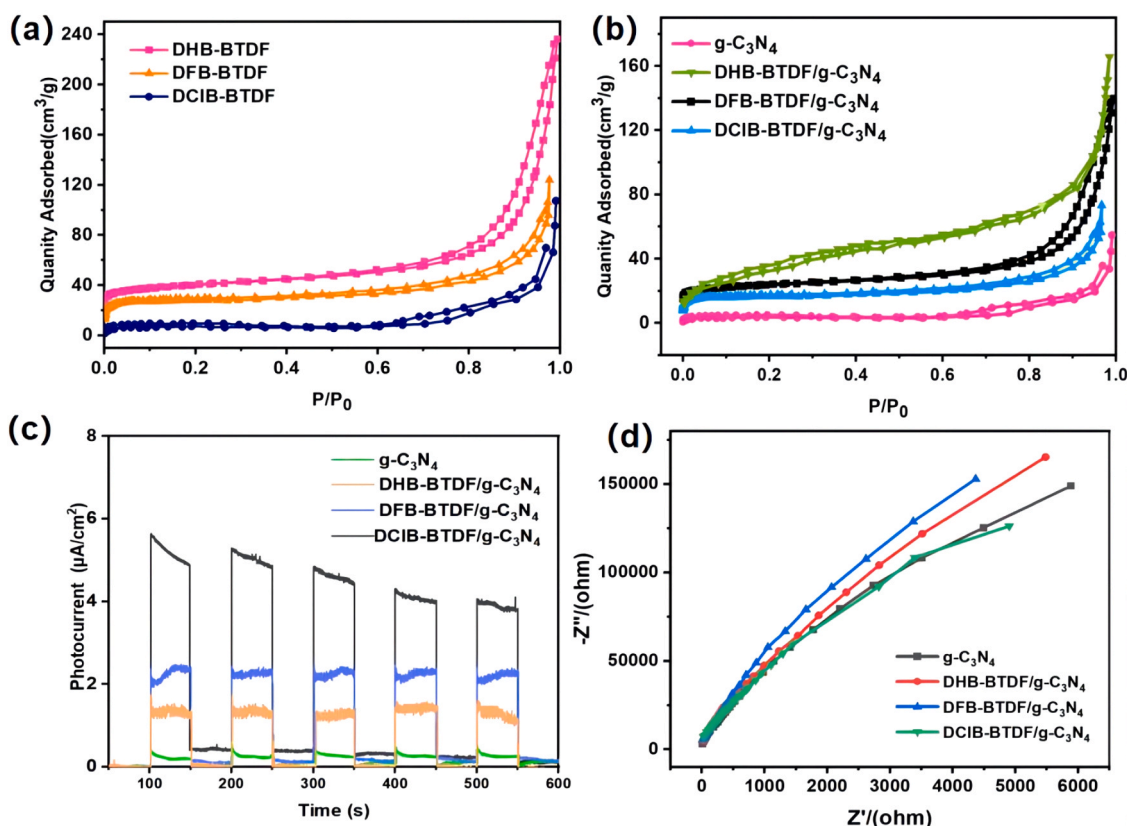


Fig. 4. (a) N₂-adsorption-desorption isotherm of the DXB-BTDF and (b) the g-C₃N₄, DXB-BTDF/g-C₃N₄ heterojunction; (c) Transient current responses to full time and on-off cycles photocurrent of illumination on the g-C₃N₄, DXB-BTDF/g-C₃N₄ heterojunction membrane electrodes; (d) EIS Nyquist plots of g-C₃N₄, DXB-BTDF/g-C₃N₄ heterojunction.

Table 1
Screening of optimal reaction conditions ^a.

Entry	Catalyst	Conv. (%) ^b	Sel. (%) ^b
1	g-C ₃ N ₄	<5	93
2	DHB-BTDF	27	95
3	DFB-BTDF	38	95
4	DCIB-BTDF	46	96
5	DHB-BTDF/ g-C ₃ N ₄	87	98
6	DFB-BTDF/ g-C ₃ N ₄	93	98
7	DCIB-BTDF/ g-C ₃ N ₄	98	99

^a Reaction conditions: 1 mmol substrate, 20 mg of catalyst, 5 mL of MeCN/H₂O, 3.5 h, blue LEDs (3 W × 4), 1 atm of O₂.

^b Confirmed by GC and GC-MS, conversion of phenyl methyl sulfide, selectivity of phenyl methyl sulfoxide.

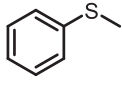
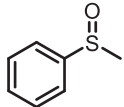
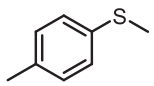
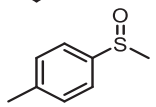
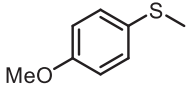
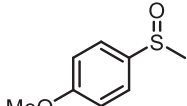
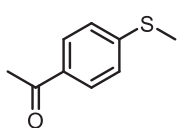
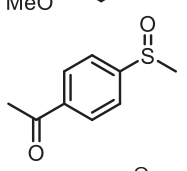
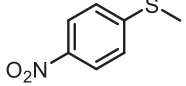
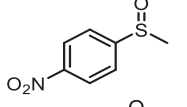
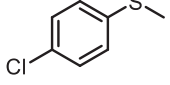
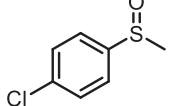
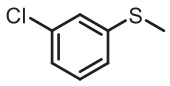
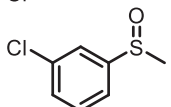
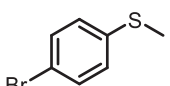
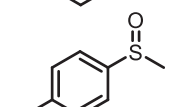
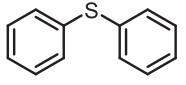
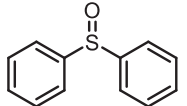
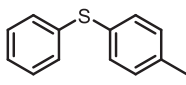
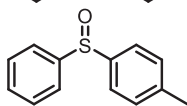
can broaden the spectrum to the visible light region. Furthermore, the optical band gap energies (E_g) of the samples were determined from the equation: $(\alpha h\nu)^2 = A(h\nu - E_g)$. According to the onset of the curved edges, the E_g values of g-C₃N₄ and DXB-BTDF/g-C₃N₄ were calculated as 2.67, 2.58, 2.61 and 2.65 eV, respectively (Fig. 1e). Compared with that of g-C₃N₄, three polymer/g-C₃N₄ heterojunctions had the narrower E_g , which indicated that they had the more significant optical adsorption and were beneficial for electron transfer from polymers to g-C₃N₄, suppressing the recombination of electron and hole effectively. The Mott-Schottky plot indicated that the g-C₃N₄ and DXB-BTDF polymers acted as n-type semiconductors. The calculated flat-band potentials of

DXB-BTDF and g-C₃N₄ were -1.02 V, -1.05 V, -1.08 V, and -1.07 V, respectively, versus NHE at pH = 7 (Fig. S2). According to the band gap energies and the CB position of the samples [55], we could paint the band gap structures as displayed in Fig. 1f. It should be noted that all CB of DXB-BTDF are lower than the oxygen reduction potential, which makes them suitable for reducing the oxygen to superoxide in solution theoretically. DCIB-BTDF/g-C₃N₄ shows the highest VB position in the three heterojunction polymers which endows its strongest oxidation ability of photogenerated holes.

The charge density distribution and the calculated HOMO and LUMO of DXB-BTDF by Gaussian are shown in Fig. S3 and Table S4. The HOMO-LUMO gap obtained has a certain positive correlation with the optical gap calculated by Uv-vis in actual experiments [50,51]. With the introduction of halogen atoms, the band gap of polymers shows an upward trend in both theoretical calculations and practical experiments. HOMO-LUMO gap has the same trend as the optical gap, and these data also support the accuracy of our work.

The thermal stability of polymer/g-C₃N₄ heterojunctions and g-C₃N₄ was studied by thermogravimetric analysis (Fig. S4). The TG curve clearly shows that g-C₃N₄ has the best thermal stability under nitrogen conditions, with only 19.8 % weight loss at 600 °C. Polymer/g-C₃N₄ heterojunctions are less stable than g-C₃N₄, DHB-BTDF/g-C₃N₄ and DFB-BTDF/g-C₃N₄ still maintain their quality at 800 °C temperature of more than 40 %. The stability of DCIB-BTDF/g-C₃N₄ is slightly worse than other polymer/g-C₃N₄ series, and it can also be seen that the thermal stability of the polymer decreases slightly after the introduction of electron-absorbing groups. In order to further study the surface composition and binding state of polymer/g-C₃N₄ elements, X-ray photoelectron spectroscopy (XPS) was used for element analysis and surface chemical state. As can be seen from Fig. 2a, the main elements of pure g-C₃N₄ and polymer/g-C₃N₄ heterojunctions are carbon (C),

Table 2Photo-oxidation of different sulfides by DCIB-BTDF/g-C₃N₄.^a

Entry	Substrate	Product	Time (h)	Conv. (%) ^b	Sel. (%) ^b
1			3.5	98	99
2			3	95	98
3			3	91	99
4			4	92	97
5			5	50	99
6			4	90	96
7			5	93	98
8			4	90	98
9			6	88	98
10			6.5	90	98

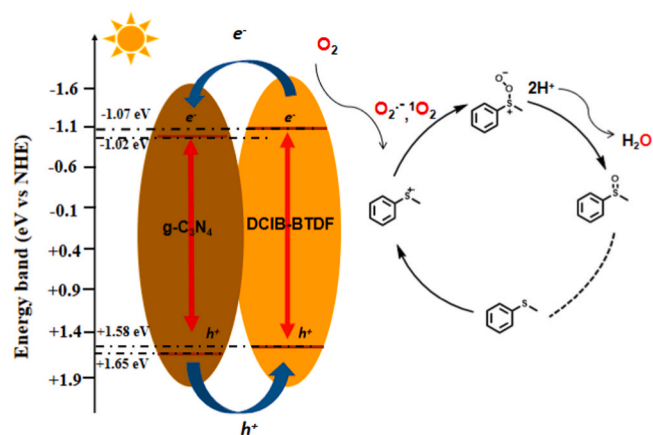
^a Reaction conditions: 2 mmol substrate, 10 mg of catalyst, 5 mL of CH₃CN/H₂O, 3.5 h, RT, blue LEDs (3 W × 4), 1 atm of O₂.^b Determined by GC and GC-MS.**Table 3**Photosulfoxidation reaction with the reactive species scavenger.^a

Entry	DCIB-BTDF/g-C ₃ N ₄	hν	O ₂	Scavenger	Inhibited species	Conversion (%) ^b
1	-	+	+	-	-	<1
2	+	-	+	-	-	<1
3	+	+	N ₂	-	-	<1
4	+	+	+	p-BQ	O ₂ ^{•-}	47
5	+	+	+	Edta ₂ Na	hole	43
6	+	+	+	DABCO	¹ O ₂	35
7	+	+	+	AgNO ₃	Electron	80
8	+	+	+	isopropanol	•OH	85

^a Reaction conditions: 2 mmol substrate, 10 mg of catalyst, 5 mL of CH₃CN/H₂O, 3.5 h, RT, blue LEDs (3 W × 4), 1 atm of O₂.^b Determined by GC and GC-MS.

nitrogen (N) and a small amount of oxygen (O). Due to the presence of a carbon-containing aromatic ring structure in DXB-BTDF, the C/N of the polymer/g-C₃N₄ heterojunctions are much higher than that of pure g-C₃N₄ (Table S1). In g-C₃N₄ and polymer/g-C₃N₄ heterojunctions, the main N element comes from g-C₃N₄. It is worth noting that the binding energies of the N1s XPS peaks of polymer/g-C₃N₄ heterojunctions were detected to be lower compared with g-C₃N₄. Based on previous work on composite heterojunctions, this may be the result of an increase in the density of electron clouds around the N atoms of graphite-phase carbon nitride [52,53], it is shown that there is intermolecular electron diffusion from polymer to graphite at the N site through the intermolecular π-π interaction.

Furthermore, XPS spectra of F1s and Cl2p (8.0 % and 6.5 %) were observed in DFB-BTDF/g-C₃N₄ and DCIB-BTDF/g-C₃N₄ samples due to the introduction of fluorine and chlorine atoms. Polymer/g-C₃N₄ heterojunctions displayed two new peaks at 287.4 and 287.3 eV, which corresponded to C-F and C-Cl bonds because of the introduction of halogens. The high-resolution XPS spectra of C 1s in the g-C₃N₄ and



Scheme 2. Proposed mechanism for the photo-oxidation of sulfoxides to sulfones under visible light conditions.

polymer/g-C₃N₄ heterojunctions are presented in Fig. 2b. Two main peaks of g-C₃N₄ and polymer/g-C₃N₄ heterojunctions were deconvoluted into superficial amorphous C (C-C/C=C, 285.6 eV), and the sp² hybridization in s-triazine units (C-N = C, 289.0 eV) [54], and their binding energy are 285.40 eV and 288.7 eV for DHB-BTDF/g-C₃N₄, 285.5 eV and 289.0 eV for DFB-BTDF/g-C₃N₄, 285.5 eV and 288.9 eV for DCIB-BTDF/g-C₃N₄, respectively. As is well known, binding energy had negative correlation with charge density [55]. With the introduction of g-C₃N₄, the binding energies of C=C and C-N = C in polymer/g-C₃N₄ heterojunctions decreased, indicating a tendency for g-C₃N₄ to transfer electrons to polymers. In addition, only had g-C₃N₄ closely contact with polymers, the internal electric field to electron transfer can formed.

Similarly, the lower binding energy of N1s XPS peaks in three polymer/g-C₃N₄ heterojunctions was detected compared to pure g-C₃N₄. This close integration was further confirmed from the changed binding energy of N 1s (Fig. 2c) [56]. Fig. 2d shows an overlap of two kinds of F1s peaks at 684.3 and 686.1 eV, which could be identified as the physically absorbed or entrapped F atoms [57] and the C-F bonds that have been revealed in its Cl1s spectrum [58]. As shown in Fig. 2e, the Cl 2p at 198.3 and 200.2 eV can be assigned to N-Cl and C-Cl groups [59], respectively, indicating that chlorine covalently bonded with carbon and nitrogen in the polymers.

After doping with halogens, both C-N = C and C-C=N peaks of DFB-BTDF/g-C₃N₄ and DCIB-BTDF/g-C₃N₄ were shifted to the larger binding energy. Steady-state photoluminescence (PL) spectroscopy was implemented to specify photophysical characteristics of the photogenerated electron holes (Fig. 2f). With the introduction of g-C₃N₄ and halogen atoms (F, Cl), the fluorescence characteristic peaks of DXB-BTDF/g-C₃N₄ all exhibit gradual blue-shift in visible-light range. The PL intensity of

the three polymer/g-C₃N₄ heterojunctions is lower than the original polymers, demonstrating that there is an effective charge transfer and inhibited the recombination efficiency of carriers between polymers and g-C₃N₄.

The surface morphologies of DXB-BTDF compounds obtained by scanning electron microscopy (Fig. S5) are rod-like as shown. At the same time, data stream-data streams and DCIB-BTDF exhibit a higher degree of nanorod agglomeration. Further characterization of polymers by transmission electron microscopy analysis. The surface morphology of DXB-BTDF obtained with SEM and TEM (Fig. 3), it could be observed that all polymers show rod-like structure, while DFB-BTDF and DCIB-BTDF exhibit a higher degree of nanorod agglomeration. As shown in Fig. 3a, the g-C₃N₄ exhibits a wrinkled structure with curled edges. After forming a heterojunction with g-C₃N₄, all polymer/g-C₃N₄ heterojunctions have a denser band-like morphology than g-C₃N₄ (Fig. 3b-d), TEM further characterized that the polymer heterojunctions are ribbon-like and rod-like forms crossed, which illustrates the successful synthesis of the polymers and g-C₃N₄ (Fig. 3f-h).

Fig. 4a shows the nitrogen adsorption-desorption isotherms of DXB-BTDF. All polymers exhibit typical Type IV isotherms, demonstrating a mesoporous structure. The specific surface areas of DHB-BTDF, DFB-BTDF and DCIB-BTDF were 187.78 m² g⁻¹, 121.24 m² g⁻¹ and 105.56 m² g⁻¹, respectively. Interestingly, the porous structure of all linear polymers may be caused by the distortion and packing of molecular chains, resulting in the formation of certain pores in the solid, and the introduction of halogen atoms of F or Cl resulting in a decrease in the polymer surface area. Fig. 4b shows nitrogen adsorption-desorption isotherms for g-C₃N₄ and DXB-BTDF/g-C₃N₄. The specific surface area decreased from 206.48 m² g⁻¹ (g-C₃N₄) to 123.74 m² g⁻¹ (DCIB-BTDF/g-C₃N₄), DHB-BTDF/g-C₃N₄ and DCIB-BTDF/g-C₃N₄ had a specific surface area of 147.73 m² g⁻¹ and 140.28 m² g⁻¹ (Table S2). This suggests that introducing linear polymers into the g-C₃N₄ frame may block pore size and reduce specific surface area. However, due to the introduction of g-C₃N₄, the specific surface area of DCB-BTDF/g-C₃N₄ are increased compared to that of the original polymer. These results once again confirm the successful combination of g-C₃N₄ and polymers, with an increased surface area that can adsorb more reactants and significantly improve the conversion rate. Compared to g-C₃N₄ and DXB-BTDF, the photocurrent density of all three DXB-BTDF/g-C₃N₄ increased, and DCIB-BTDF/g-C₃N₄ had the highest photocurrent density. As expected, the trend of photocurrent generation followed the order of photocatalytic properties, indicating that the construction of heterostructures and introducing halogen atoms into polymers can effectively accelerate the separation and transfer of electrons and holes (Fig. 4c). The charge transfer rate was further characterized by EIS measurement. With the introduction of F and Cl atoms, the semicircle of DCIB-BTDF/g-C₃N₄ in the Nyquist plot showed a significantly reduced radius (Fig. 4d), indicating a lowest charge transfer resistance and higher charge mobility.

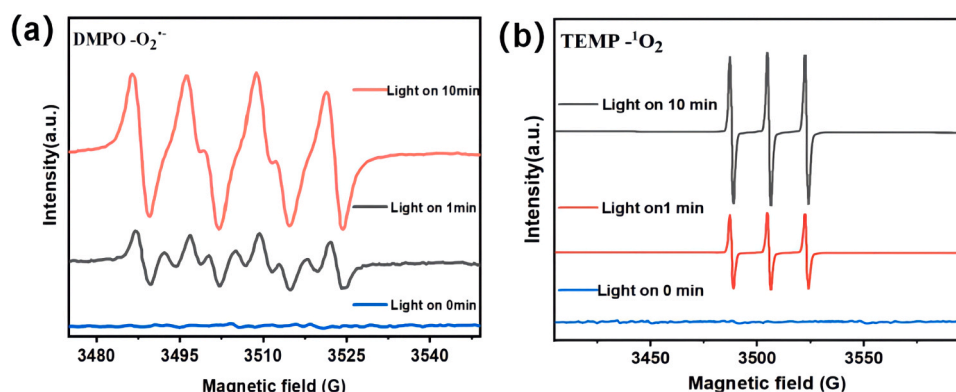


Fig. 5. (a) Spin trapping of O₂^{•-} with DMPO; (b) spin trapping of ¹O₂ with TEMP in the blue light-induced selective oxidation of DCIB-BTDF/g-C₃N₄.

3.2. Photocatalytic performance

Sulfoxides are vital pharmaceutical intermediates, and visible light-induced selective oxidation of sulfides is an important route to obtain sulfoxides, featuring mild reaction conditions, atom economy, and environmental friendliness [60–62]. By using thioanisole as the model substrate, we took the variable control method to select the important and optimal factors: different wavelengths of LEDs (Table S3) and different solvents (Fig. S6). It was unveiled that under the irradiation of 460 nm blue LEDs and protic solvents MeCN/H₂O was efficient for the selective aerobic oxidation of sulfides into sulfoxides by DCIB-BTDF. The performance of various catalysts was investigated. Pure g-C₃N₄ was only achieved a negligible conversion (Entry 1, Table 1). DCIB-BTDF exhibited a 46 % yield in 3.5 h (Entry 4, Table 1). The combination of g-C₃N₄ and DXB-BTDF, which formed a heterojunction photocatalyst, led to the extensive increase in the yield of DXB-BTDF (Entry 5–7, Table 1). This enhanced photocatalytic activity corresponded to the increase separation efficiency of the photogenerated carriers. Note that the photocatalytic activities of the DXB-BTDF/g-C₃N₄ series were well matched with their photoelectrochemical properties. The conversion of DCIB-BTDF/g-C₃N₄ might reach > 98 % with a selectivity above 99 % when MeCN/H₂O is used as a solvent in 3.5 h (Entry 7, Table 1).

The excellent photocatalytic activity of DCIB-BTDF/g-C₃N₄ prompted us to further explore its scope of application in the selective oxidation of sulfides with the optimal conditions. Compared to other heterogeneous photocatalysts (Table S5), the performance of DCIB-BTDF/g-C₃N₄ is outstanding for the selective oxidation of phenyl methyl sulfide. Benzyl sulfides (Table 2, Entry 2–4) which electron-donating groups substitute were easier oxidized than phenyl methyl sulfides (Table 2, Entry 1), and the electron-withdrawing groups substituted benzyl sulfides were slightly slower (Table 2, entries 6–8), apart from the strong electron-withdrawing substituents (Table 2, Entry 5). For diphenyl sulfide, it takes longer reaction time to transform because of the steric hindrance of the substituted phenyl groups (Table 2, entries 9–10). These results unveil that both the electronic effect and steric effect produce a significant impact on the substrate conversion. The DCIB-BTDF/g-C₃N₄ polymer exhibited nice recyclability and stability with little change in the relative activity after five runs (Fig. S7), and at this stage the peaks in the FT-IR spectrum of the photocatalyst were slightly attenuated, the SEM showed that the catalyst structure or framework had been slightly degraded (Fig. S8).

3.3. Mechanism investigation

To determine the reactive oxygen species (ROS), a series of quenching experiments were first carried out by introducing various scavengers, and the results were displayed in Table 3. The reaction did not occur in the absence of the photocatalyst, light irradiation, or oxygen (Table 3, entries 2–4). We used isopropanol as •OH scavenger and AgNO₃ as an electron scavenger and clear difference in the product yields was not observed. However, a sharply decreased conversion of thioanisole with the addition of p-BQ as an O₂•⁻ scavenger, DABCO as an ¹O₂ scavenger and Edta₂Na as a hole trapping agent, demonstrating its crucial roles for the oxidation. Therefore, based on the above results and preceding studies, a plausible photocatalytic reaction mechanism is proposed in Scheme 2. Under blue light irradiation, the electrons of DCIB-BTDF/g-C₃N₄ migrate from HOMO to LUMO, producing separated electron-hole pairs. In the electron transfer pathway, holes obtain an electron from benzyl sulfide to form an S-center radical cation intermediate. Accordingly, Oxygen was activated to ¹O₂ and O₂•⁻ by the photogenerated charges. Further, O₂•⁻ and ¹O₂ attack the phenyl methyl sulfide radical cation to generate the final product sulfoxide. To further confirm the free radicals generated from the photocatalytic system, EPR measurements for trapping the transient-state radical were conducted. DMPO was added as a radical trapping reagent of ROS as well as alkyl and N-containing free radicals. The characteristic spectrum of the O₂•⁻

signal (1:2:2:1) was recorded after illumination (Fig. 5a). In addition, 2,2,6,6-tetramethylpiperidine (TEMP) was used as the ¹O₂ trapper in the photocatalytic system. The characteristic triplet peak signal (1:1:1) was observed (Fig. 5b). Similarly, no EPR signal was not observed for benzylamine cationic radicals when reaction in the dark. (Fig. S9).

4. Conclusion

In summary, this study presented a new designed molecular strategy proposed to improve selective oxidation of heterojunction. We successfully synthesized a series of organic conjugated polymers of DXB-BTDF and polymer/g-C₃N₄ heterojunctions were further constructed via π–π stacking. After an elaborate investigation, it was shown that the incorporation of g-C₃N₄ into the DXB-BTDF might simultaneously improve the light-harvesting capacity, bandgap structure, separation efficiency and interfacial transfer rate of photogenerated charge carriers owing the electrostatic attraction between g-C₃N₄ and DXB-BTDF. DCIB-BTDF/g-C₃N₄ heterojunctions exhibited superior photocatalytic activity under visible-light illumination for the aerobic selective oxidation of sulfides under visible light irradiation in comparison to the pristine DCIB-BTDF and other DXB-BTDF (X = H, F) series. The highest activity achieved on the DCIB-BTDF might reach > 98 % of conversion, which was more than 2 times higher than that of pristine DCIB-BTDF. The construct of heterojunction structure and halogenation strategy provide further insight for designing and synthesizing the organic polymer heterojunctions to obtain efficient and stable photocatalysts.

CCRediT authorship contribution statement

Chu Chu: Data curation, Formal analysis. **Yuancheng Qin:** Methodology, Data curation, Formal analysis. **Cailing Ni:** Formal analysis. **Nannan Wu:** Formal analysis. **Jianping Zou:** Conceptualization, Supervision, Methodology, Data curation, Formal analysis, Visualization, Writing – review & editing.

Declaration of Competing Interest

The authors declare that they have no known competing financial interests or personal relationships that could have appeared to influence the work reported in this paper.

Data availability

All data that support the findings of this study are included in this manuscript and is supplementary information files.

Acknowledgements

This work was financially supported by National Natural Science Foundation of China (52173099, 52203262), the Natural Science Foundation of Jiangxi Province (20202BAB213005), Training Project of High-level and High-skilled Leading Talents of Jiangxi Province.

Appendix A. Supporting information

Supplementary data associated with this article can be found in the online version at doi:10.1016/j.apcatb.2023.123321.

References

- [1] B.P.J. Andree, A. Chamorro, P. Spencer, E. Koomen, H. Dogo, Revisiting the relation between economic growth and the environment; a global assessment of deforestation, pollution and carbon emission, *Renew. Sustain. Energy Rev.* 114 (2019), 109221.
- [2] H.L. Wang, L.S. Zhang, Z.G. Chen, J.Q. Hu, S.J. Li, Z.H. Wang, J.S. Liu, X.C. Wang, Semiconductor heterojunction photocatalysts: design, construction, and photocatalytic performances, *Chem. Soc. Rev.* 43 (2014) 5234–5244.

- [3] Y. Zheng, L.H. Lin, B. Wang, X.C. Wang, Graphitic carbon nitride polymers toward sustainable photoredox catalysis, *Angew. Chem. Int. Ed.* 54 (2015) 12868–12884.
- [4] T. Banerjee, K. Gottschling, G. Savasci, C. Ochsenfeld, B.V. Lotsch, H₂ evolution with covalent organic framework photocatalysts, *ACS Energy Lett.* 3 (2018) 400–409.
- [5] M. Mansoorianfar, H. Nabipour, F. Pahlevani, Y.W. Zhao, Z. Hussain, A. Hojjati-Najafabadi, H.Y. Hoang, R.J. Pei, Recent progress on adsorption of cadmium ions from water systems using metal-organic frameworks (MOFs) as an efficient class of porous materials, *Environ. Res.* 214 (2022), 114113.
- [6] X.C. Wang, K. Maeda, A. Thomas, K. Takanabe, G. Xin, J.M. Carlsson, K. Domen, M. Antonietti, A metal-free polymeric photocatalyst for hydrogen production from water under visible light, *Nat. Mater.* 8 (2009) 76–80.
- [7] K. Kondo, N. Murakami, C. Ye, T. Tsubota, T. Ohno, Development of highly efficient sulfur-doped TiO₂ photocatalysts hybridized with graphitic carbon nitride, *Appl. Catal. B Environ.* 142 (2013) 362–367.
- [8] X.N. Yu, S.F. Ng, L.K. Putri, L.L. Tan, A.R. Mohamed, W.J. Ong, Point-defect engineering: leveraging imperfections in graphitic carbon nitride (g-C₃N₄) photocatalysts toward artificial photosynthesis, *Small* 17 (2021) 48.
- [9] Y.J. Zhou, L.X. Zhang, J.J. Liu, X.Q. Fan, B.Z. Wang, M. Wang, W.C. Ren, J. Wang, M.L. Li, J.L. Shi, Brand new P-doped g-C₃N₄: enhanced photocatalytic activity for H₂ evolution and Rhodamine B degradation under visible light, *J. Mater. Chem. A* 3 (2015) 3862–3867.
- [10] J. Kang, Y.W. Tang, M. Wang, C.Y. Jin, J.Y. Liu, S.Y. Li, Z.L. Li, J.W. Zhu, The enhanced peroxydisulfate-assisted photocatalytic degradation of tetracycline under visible light by g-C₃N₄/Na-BiVO₄ heterojunction catalyst and its mechanism, *J. Environ. Chem. Eng.* 9 (2021), 105524.
- [11] J. Jia, W.J. Sun, Q.Q. Zhang, X.Z. Zhang, X.Y. Hu, E.Z. Liu, J. Fan, Inter-plane heterojunctions within 2D/3D FeSe₂/g-C₃N₄ nanosheet semiconductors for photocatalytic hydrogen generation, *Appl. Catal. B Environ.* 261 (2020), 118249.
- [12] M. Nemiwal, T.C. Zhang, D. Kumar, Recent progress in g-C₃N₄, TiO₂ and ZnO based photocatalysts for dye degradation: strategies to improve photocatalytic activity, *Sci. Total Environ.* 767 (2021), 144896.
- [13] J.Y. Qin, H.P. Zeng, Photocatalysts fabricated by depositing plasmonic Ag nanoparticles on carbon quantum dots/graphitic carbon nitride for broad spectrum photocatalytic hydrogen generation, *Appl. Catal. B Environ.* 209 (2017) 161–173.
- [14] W. Chen, J. Huang, Z.C. He, X. Ji, Y.F. Zhang, H.L. Sun, K. Wang, Z.W. Su, Accelerated photocatalytic degradation of tetracycline hydrochloride over CuAl₂O₄/g-C₃N₄ p-n heterojunctions under visible light irradiation, *Sep. Purif. Technol.* 277 (2021), 119461.
- [15] M.Q. Liu, Y.Y. Jiao, J.C. Qin, Z.J. Li, J.S. Wang, Boron doped g-C₃N₄ nanodots/nonmetal element (S, P, F, Br) doped g-C₃N₄ nanosheets heterojunction with synergistic effect to boost the photocatalytic hydrogen production performance, *Appl. Surf. Sci.* 541 (2021), 148558.
- [16] Z.H. Huang, H. Chen, L. Zhao, X. He, Y.Y. Du, W. Fang, W.X. Li, P. Tian, Constructing g-C₃N₄ quantum dots modified g-C₃N₄/GO nanosheet aerogel for UV-Vis-NIR driven highly efficient photocatalytic H₂ production, *Int. J. Hydrog. Energy* 44 (2019) 31041–31052.
- [17] K.L. Chen, S.S. Zhang, J.Q. Yan, W. Peng, D.P. Lei, J.H. Huang, Excellent visible light photocatalytic efficiency of Na and S co-doped g-C₃N₄ nanotubes for H₂ production and organic pollutant degradation, *Int. J. Hydrog. Energy* 44 (2019) 31916–31929.
- [18] Z.N. Lei, X.F. Cao, J. Fan, X.Y. Hu, J. Hu, N. Li, T. Sun, E.Z. Liu, Efficient photocatalytic H₂ generation over In₂Te₂/S₄/NiS₂/g-C₃N₄ S-scheme heterojunction using NiS₂ as electron-bridge, *Chem. Eng. J.* 457 (2023) 4601–4613.
- [19] X.W. Lan, Q. Li, Y.Z. Zhang, Q. Li, L. Ricardez-Sandoval, G.Y. Bai, Engineering donor-acceptor conjugated organic polymers with boron nitride to enhance photocatalytic performance towards visible-light-driven metal-free selective oxidation of sulfides, *Appl. Catal. B Environ.* 277 (2020), 119274.
- [20] W. Zou, X.H. Liu, C. Xue, X.T. Zhou, H.Y. Yu, P. Fan, H.B. Ji, Enhancement of the visible-light absorption and charge mobility in a zinc porphyrin polymer/g-C₃N₄ heterojunction for promoting the oxidative coupling of amines, *Appl. Catal. B Environ.* 285 (2021), 119863.
- [21] C.H. Dai, B. Liu, Conjugated polymers for visible-light-driven photocatalysis, *Energy Environ. Sci.* 13 (2020) 24–52.
- [22] T. Zhang, G.L. Xing, W.B. Chen, L. Chen, Porous organic polymers: a promising platform for efficient photocatalysis, *Mater. Chem. Front.* 4 (2020) 332–353.
- [23] T.X. Wang, H.P. Liang, D.A. Anito, X.S. Ding, B.H. Han, Emerging applications of porous organic polymers in visible-light photocatalysis, *J. Mater. Chem. A* 8 (2020) 7003–7034.
- [24] Z.W. Zhang, J. Jia, Y.F. Zhi, S. Ma, X.M. Liu, Porous organic polymers for light-driven organic transformations, *Chem. Soc. Rev.* 51 (2022) 2444–2490.
- [25] C. Chu, Y.C. Qin, C.L. Ni, J.P. Zou, Halogenated benzothiadiazole-based conjugated polymers as efficient photocatalysts for dye degradation and oxidative coupling of benzylamines, *Chin. Chem. Lett.* 33 (2022) 2736–2740.
- [26] B. Guo, H.X. Li, C.H. Zha, D.J. Young, H.Y. Li, J.P. Lang, Visible-light-enhanced suzuki-miyaura reactions of aryl chlorides in water with Pd NPs supported on a conjugated nanoporous polycarbazole, *ChemSusChem* 12 (2019) 1421–1427.
- [27] L.W. Xing, J.R. Liu, X. Hong, K.N. Houk, C.K. Luscombe, An exception to the carothers equation caused by the accelerated chain extension in a Pd/Ag cocatalyzed cross dehydrogenative coupling polymerization, *J. Am. Chem. Soc.* 144 (2022) 2311–2322.
- [28] P.F. Wei, M.Z. Qi, Z.P. Wang, S.Y. Ding, W. Yu, Q. Liu, L.K. Wang, H.Z. Wang, W. K. An, W. Wang, Benzoxazole-linked ultrastable covalent organic frameworks for photocatalysis, *J. Am. Chem. Soc.* 140 (2018) 4623–4631.
- [29] X.Y. Dong, H.M. Hao, F.L. Zhang, X.J. Lang, Blue light photocatalysis of carbazole-based conjugated microporous polymers: aerobic hydroxylation of phenylboronic acids to phenols, *Appl. Catal. B Environ.* 309 (2022), 121210.
- [30] J. Chen, X.P. Tao, L. Tao, H. Li, C.Z. Li, X.L. Wang, C. Li, R.G. Li, Q.H. Yang, Novel conjugated organic polymers as candidates for visible-light-driven photocatalytic hydrogen production, *Appl. Catal. B Environ.* 241 (2019) 461–470.
- [31] B. Chen, N. Yang, P. Wang, Y.G. Xiang, H. Chen, Post-side chain engineering of difluorinated benzothiadiazole-based conjugated microporous polymer for enhanced photocatalytic H₂ evolution, *Appl. Surf. Sci.* 499 (2020), 143865.1–143865.8.
- [32] X.X. Yu, Z.Z. Yang, B. Qiu, S.E. Guo, P. Yang, B. Yu, H.Y. Zhang, Y.F. Zhao, X. Z. Yang, B.X. Han, Z.M. Liu, Eosin Y-functionalized conjugated organic polymers for visible-light-driven CO₂ reduction with H₂O to CO with high efficiency, *Angew. Chem. Int. Ed.* 58 (2019) 632–636.
- [33] K. Duan, J. Wang, Y.T. Zhang, J.D. Liu, Covalent organic frameworks (COFs) functionalized mixed matrix membrane for effective CO₂/N₂ separation, *J. Membr. Sci.* 572 (2019) 588–595.
- [34] X. Liang, Z.F. Guo, H.X. Wei, X. Liu, H. Lv, H.Z. Xing, Selective photooxidation of sulfides mediated by singlet oxygen using visible-light-responsive coordination polymers, *Chem. Commun.* 54 (2018) 13002–13005.
- [35] X.T. Hu, R. Datt, Q. He, P. Kafourou, H.K.H. Lee, A.J.P. White, W.C. Tsoi, M. Heeney, Facile synthesis of annulated benzothiadiazole derivatives and their application as medium band gap acceptors in organic photovoltaic devices, *J. Mater. Chem. C* 10 (2022) 9249–9256.
- [36] L.L. An, Y.B. Huang, X. Wang, Z.Z. Liang, J.F. Li, J.F. Tong, Fluorination effect for highly conjugated alternating copolymers involving thienylenevinylene-thiophene-flanked benzodithiophene and benzothiadiazole subunits in photovoltaic application, *Polymers* 12 (2020) 504.
- [37] D. He, F.W. Zhao, L. Jiang, C.R. Wang, A-D-A small molecule acceptors with ladder-type arenes for organic solar cells, *J. Mater. Chem. A* 6 (2018) 8839–8854.
- [38] Z. Ji, W.R. Zhao, L.Y. Xiang, J.M. Ding, D.Y. Wang, X.J. Dai, L.Y. Liu, F.J. Zhang, Y. Zou, C.A. Di, Hierarchical heterojunction enhanced photodoping of polymeric semiconductor for photodetection and photothermoelectric applications, *ACS Mater. Lett.* 4 (2022) 815–822.
- [39] L.P. Xu, B.N. Tian, T.Y. Wang, Y. Yu, Y.C. Wu, J.W. Cui, Z.N. Cao, J.H. Wu, W. K. Zhang, Q. Zhang, J.Q. Liu, Z.F. Li, Y. Tian, Direct Z-scheme polymeric heterojunction boosts photocatalytic hydrogen production via a rebuilt extended pi-delocalized network, *Energy Environ. Sci.* 15 (2022) 5059–5068.
- [40] Y.B. Tang, H. Zheng, X.B. Zhou, Z. Tang, W. Ma, H. Yan, Molecular doping increases the semitransparent photovoltaic performance of dilute bulk heterojunction film with discontinuous polymer donor networks, *Small Methods* 6 (2022) 20157.
- [41] C.C. Cao, H.T. Wang, D.S. Qiu, T.X. Zhao, Y.L. Zhu, X. Lai, M.R. Pu, Y. Li, H. Li, H. Chen, F. He, Quasiplanar heterojunction all-polymer solar cells: a dual approach to stability, *Adv. Funct. Mater.* 32 (2022) 1829–1837.
- [42] H.N. Ye, Z.Q. Wang, F.T. Yu, S.C. Zhang, K.Y. Kong, X.Q. Gong, J.L. Hua, H. Tian, Fluorinated conjugated poly(benzotriazole)/g-C₃N₄ heterojunctions for significantly enhancing photocatalytic H₂ evolution, *Appl. Catal. B Environ.* 267 (2020), 118577.
- [43] J.O. Link, J.G. Taylor, L.H. Xu, M. Mitchell, H.Y. Guo, H.T. Liu, D. Kato, T. Kirschberg, J.Y. Sun, N. Squires, J. Parrish, T. Kellar, Z.Y. Yang, C. Yang, M. Matles, Y.J. Wang, K. Wang, G.F. Cheng, Y. Tian, E. Mogalian, E. Mondou, M. Cornprost, J. Perry, M.C. Desai, Discovery of Ledipasvir (GS-5885): a potent, once-daily oral ns5a inhibitor for the treatment of Hepatitis C virus infection, *J. Med. Chem.* 59 (2016), 7696–7696.
- [44] X.J. Wang, G.F. Wang, F. Liang, Y. Wang, X. Wei, L.H. Feng, L.W. Zhang, Highly sensitive and selective chemosensors for D-fructose based on electrostatic interaction in aqueous solution, *Sens. Actuators B Chem.* 171 (2012) 486–491.
- [45] J. Kim, M.H. Yun, G.H. Kim, J. Lee, S.M. Lee, S.J. Ko, Y. Kim, G.K. Dutta, M. Moon, S.Y. Park, D.S. Kim, J.Y. Kim, C. Yang, Synthesis of PCDTBT-based fluorinated polymers for high open-circuit voltage in organic photovoltaics: towards an understanding of relationships between polymer energy levels engineering and ideal morphology control, *ACS Appl. Mater. Interfaces* 6 (2014) 7523–7534.
- [46] X. Zhu, C.C. Tian, T. Jin, J.T. Wang, S.M. Mahurin, W.W. Mei, Y. Xiong, J. Hu, X. L. Feng, H.L. Liu, S. Dai, Thiazolothiazole-linked porous organic polymers, *Chem. Commun.* 50 (2014) 15055–15058.
- [47] Y.H. Liu, J.B. Zhao, Z.K. Li, C. Mu, W. Ma, H.W. Hu, K. Jiang, H.R. Lin, H. Ade, H. Yan, Aggregation and morphology control enables multiple cases of high-efficiency polymer solar cells, *Nat. Commun.* 5 (2014) 5293–5301.
- [48] X.C. Wang, Z.R. Du, K.K. Dou, H.X. Jiang, C.L. Gao, L.L. Han, R.Q. Yang, A. Maverick, Asymmetrical Backbone with distinct flanked twist angles modulating the molecular aggregation and crystallinity for high performance nonfullerene solar cells, *Adv. Energy Mater.* 9 (2019) 0253–0264.
- [49] Y. Wu, Y. Zheng, H. Yang, C.K. Sun, Y.Y. Dong, C.H. Cui, H. Yan, Y.F. Li, Rationally pairing photoactive materials for high-performance polymer solar cells with efficiency of 16.53, *Sci. China Chem.* 63 (2020) 265–271.
- [50] M. Nakata, T. Shimazaki, PubChemQC project: a large-scale first-principles electronic structure database for data-driven chemistry, *J. Chem. Inf. Model.* 57 (2017) 1300–1308.
- [51] J. Sworakowski, How accurate are energies of HOMO and LUMO levels in small-molecule organic semiconductors determined from cyclic voltammetry or optical spectroscopy? *Synth. Met.* 235 (2018) 125–130.
- [52] F.T. Yu, Z.Q. Wang, S.C. Zhang, H.N. Ye, K.Y. Kong, X.Q. Gong, J.L. Hua, H. Tian, Molecular engineering of donor-acceptor conjugated polymer/g-C₃N₄ heterostructures for significantly enhanced hydrogen evolution under visible-light irradiation, *Adv. Funct. Mater.* 28 (2018) 4516–4529.

- [53] J. Chen, C.L. Dong, D.M. Zhao, Y.C. Huang, X.X. Wang, L. Samad, L.N. Dang, M. Shearer, S.H. Shen, L.J. Guo, Molecular design of polymer heterojunctions for efficient solar-hydrogen conversion, *Adv. Mater.* 29 (2017) 6198.
- [54] J.W. Fu, B.C. Zhu, C.J. Jiang, B. Cheng, W. You, J.G. Yu, Hierarchical porous O-doped g-C₃N₄ with enhanced photocatalytic CO₂ reduction activity, *Small* 13 (2017) 3938–3947.
- [55] J. Xiong, X.B. Li, J.T. Huang, X.M. Gao, Z. Chen, J.Y. Liu, H. Li, B.B. Kang, W. Q. Yao, Y.F. Zhu, CN/rGO@BPQDs high-low junctions with stretching spatial charge separation ability for photocatalytic degradation and H₂O₂ production, *Appl. Catal. B Environ.* 266 (2020), 118602.
- [56] X.H. Song, X. Li, X.Y. Zhang, Y.F. Wu, C.C. Ma, P.W. Huo, Y.S. Yan, Fabricating C and O co-doped carbon nitride with intramolecular donor-acceptor systems for efficient photoreduction of CO₂ to CO, *Appl. Catal. B Environ.* 268 (2020), 118736.
- [57] D.Q. Gao, Y.G. Liu, M.Y. Song, S.P. Shi, M.S. Si, D.S. Xue, Manifestation of high-temperature ferromagnetism in fluorinated graphitic carbon nitride nanosheets, *J. Mater. Chem. C* 3 (2015) 12230–12235.
- [58] N. Wang, H. Fan, J.C. Sun, Z.W. Han, J. Dong, S.Y. Ai, Fluorine-doped carbon nitride quantum dots: ethylene glycol-assisted synthesis, fluorescent properties, and their application for bacterial imaging, *Carbon* 109 (2016) 141–148.
- [59] S. Li, M.F. Wu, T. Guo, L.L. Zheng, D.K. Wang, Y. Mu, Q.J. Xing, J.P. Zou, Chlorine-mediated photocatalytic hydrogen production based on triazine covalent organic framework, *Appl. Catal. B Environ.* 272 (2020), 118989.
- [60] K.Y. Feng, H.M. Hao, F.W. Huang, X.J. Lang, C. Wang, A 2D porphyrin-based covalent organic framework with TEMPO for cooperative photocatalysis in selective aerobic oxidation of sulfides, *Mater. Chem. Front.* 5 (2021) 2255–2260.
- [61] X.J. Lang, J.C. Zhao, X.D. Chen, Visible-light-induced photoredox catalysis of dye-sensitized titanium dioxide: selective aerobic oxidation of organic sulfides, *Angew. Chem. Int. Ed.* 55 (2016) 4697–4700.
- [62] F.L. Zhang, X.M. Ma, X.Y. Dong, X. Miao, X.J. Lang, Inserting acetylene into an olefin-linked covalent organic framework for boosting the selective photocatalytic aerobic oxidation of sulfides, *Chem. Eng. J.* 451 (2023), 138802.